M₅X₄ – A Family of MXenes

Marley Downes[1], Christopher Eugene Shuck[1], Robert Lord[1], Mark Anayee[1], Mikhail Shekhirev[1], Ruocun (John) Wang[1], Tetiana Hryhorchuk[1], Martin Dahlqvist[2], Johanna Rosen[2], Yury Gogotsi[1*]

[1]*Department of Materials Science and Engineering, and A.J. Drexel Nanomaterials Institute, Drexel University, Philadelphia, Pennsylvania 19104, United States*
[2]*Materials Design Division, Department of Physics, Chemistry and Biology (IFM), Linköping University, SE-581 83 Linköping, Sweden*

*Corresponding author: gogotsi@drexel.edu

KEYWORDS: MXene, two-dimensional, MAX phase, synthesis, structure, properties

ABSTRACT

MXenes are two-dimensional (2D) transition metal carbides, nitrides, and carbonitrides typically synthesized from layered MAX-phase precursors. With over 50 experimentally reported MXenes and a near-infinite number of possible chemistries, MXenes are the fastest-growing family of 2D materials. They offer a wide range of properties, which can be altered by their chemistry (M, X, T_x) and the number of metal layers in the structure, ranging from two in M_2XT_x to five in M_5X_4. Only one $M_5X_4T_x$ MXene, Mo_4VC_4, has been reported. Herein, we report the synthesis and characterization of two new phase-pure M_5AX_4 mixed transition metal MAX-phases, $(TiTa)_5AlC_4$ and $(TiNb)_5AlC_4$, and their successful topochemical transformation into $(TiTa)_5C_4T_x$ and $(TiNb)_5C_4T_x$ MXenes. The resulting MXenes were delaminated into single-layer flakes, analyzed structurally, and characterized for their thermal and optical properties. This establishes a family of M_5AX_4 MAX phases and their corresponding MXenes. These materials were experimentally produced based on guidance from theoretical predictions, opening the door to exciting new applications for MXenes.

INTRODUCTION

MXenes are a large family of 2D materials, with more than 50 stoichiometric MXenes experimentally synthesized, hundreds of computationally predicted compositions, and an infinite number of solid-solution MXenes (Figure 1).[1,2] The general formula of MXenes can be expressed as $M_{n+1}X_nT_x$ where M is an early transition metal (Ti, Nb, Ta, Mo, V, etc.), X is carbon and/or nitrogen, and n is an integer $1 – 4$. T_x represents the surface termination groups (typically –OH, =O, and –F)[3] and will not be continually expressed for clarity. MXenes have attracted significant attention due to their coupled high volumetric capacitance[4] and high electronic conductivity,[5] biocompatibility,[6] electrochromic behavior,[7] and optical absorption peaks in the UV-NIR range;[8] this has led to their use in applications including electrochemical energy storage,[9] biomedicine,[10] optoelectronics,[11] and many others.[12,13]

MXenes are commonly synthesized through selective chemical etching from precursor MAX phases, which have the general formula $M_{n+1}AX_n$, where the A layer is comprised of group 13/14 elements (typically, Al for MXene synthesis). The monoatomic A layer is removed during the chemical etching process, leaving behind multilayer (ML) MXene flakes.[14] Delamination with organic or inorganic ions can separate the multilayer MXene particles, yielding single flakes dispersed in water, which are easily processed into films through vacuum filtration, spray-coating, spin-coating, or other methods.[15,16]
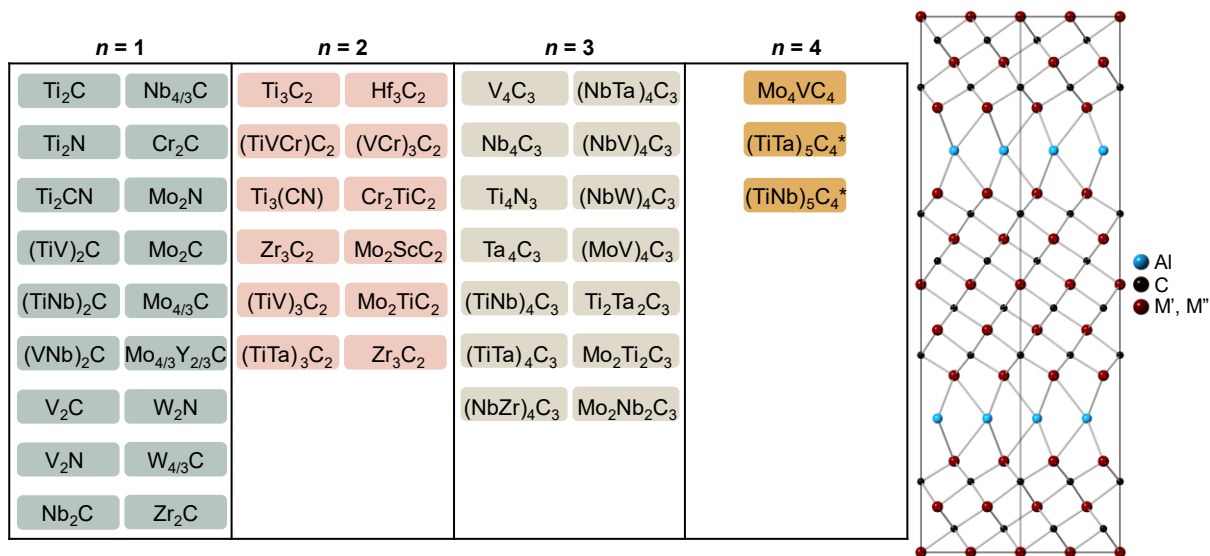
1

	$n = 1$		$n = 2$		$n = 3$		$n = 4$
Ti_2C	$Nb_{4/3}C$	Ti_3C_2	Hf_3C_2	V_4C_3	$(NbTa)_4C_3$	Mo_4VC_4	
Ti_2N	Cr_2C	$(TiVCr)C_2$	$(VCr)_3C_2$	Nb_4C_3	$(NbV)_4C_3$	$(TiTa)_5C_4$*	
Ti_2CN	Mo_2N	$Ti_3(CN)$	Cr_2TiC_2	Ti_4N_3	$(NbW)_4C_3$	$(TiNb)_5C_4$*	
$(TiV)_2C$	Mo_2C	Zr_3C_2	Mo_2ScC_2	Ta_4C_3	$(MoV)_4C_3$		
$(TiNb)_2C$	$Mo_{4/3}C$	$(TiV)_3C_2$	Mo_2TiC_2	$(TiNb)_4C_3$	$Ti_2Ta_2C_3$		
$(VNb)_2C$	$Mo_{4/3}Y_{2/3}C$	$(TiTa)_3C_2$	Zr_3C_2	$(TiTa)_4C_3$	$Mo_2Ti_2C_3$		
V_2C	W_2N			$(NbZr)_4C_3$	$Mo_2Nb_2C_3$		
V_2N	$W_{4/3}C$						
Nb_2C	Zr_2C						

Figure 1. Synthesized MXenes reported to date, including eighteen M_2X,[5,17–26] twelve M_3X_2,[1,26–31] fourteen M_4X_3,[26,27,30,32–35] and three M_5X_4.[36] Beyond these listed MXenes are in-plane ordered, various solid-solution compositions, high-entropy, and other related materials.[30,37,38] Two new MXenes with $n = 4$ are reported here and marked with stars. Additional MAX-phases discovered in this study but not exfoliated into MXenes are shown in the Supporting Information. The crystal structure of the M_5AX_4 lattice with space group $P6_3/mmc$ is shown along the [110] plane.

While MXenes have the general formula $M_{n+1}X_nT_x$, the metallic component (M) can include two or more metals. Generally, these MXenes can be divided into ordered MXenes or solid solution MXenes.[2] The ordered MXenes exhibit ordering in one of two ways: in-plane (*i*-MXene) or out-of-plane (*o*-MXene). In-plane ordering is only found in $(M'_{4/3}M''_{2/3})CT_x$ structures (M' = Mo, W, V, Cr; M'' = Sc, Zr or Y, or some lanthanides)[39] and has alternating rows of the M-metals within the planes. Out-of-plane ordering is found in the $M_2'M''C_2T_x$ and $M_2'M_2''C_3T_x$ structures with M' in the outer layer, and M'' in the inner layer(s), such as $Mo_2Ti_2C_3T_x$, $Mo_2TiC_2T_x$, $Mo_2ScC_2T_x$, or $Cr_2TiC_2T_x$.[40] Solid solution MXenes, on the other hand, have random ordering of either the X-site or the M-site. Solid solution on the X site includes MXenes such as Ti_3CN, where the carbon and nitrogen randomly occupy the octahedral sites typically only occupied by carbon.[41] Solid solution on the M-site contains MXenes that have a random occupation of the M-sites. M-site solid solution is the largest predicted family as there are a near-infinite number of combinations across the periodic table to create novel MXenes. A large variety of solid solution MXenes have been reported, including $Ti_{2-y}Nb_yCT_x$, $Ti_{2-y}V_yCT_x$,[5] and $Mo_{4-y}V_yC_3T_x$[42], among many others. To date, $M_5X_4T_x$ MXene only has an M-site solid-solution structure.

MXenes are further divided into families based on the number of atomic layers: M_2X, M_3X_2, M_4X_3, and, most recently, M_5X_4. The first phase-pure higher-ordered MAX phase ($n > 3$) was reported in 2019 to be Mo_4VAlC_4 with accompanying MXene Mo_4VC_4, establishing that phase-pure higher-ordered MAX phases and MXenes could be successfully synthesized.[36] This family of MXenes is important because M_5X_4 ($n = 4$) demonstrates unique properties that are not found in other MXenes ($n = 1 – 3$). It was shown that they have the highest thermal stability of any MXene to date (~1000 vs < 800 °C for other MXenes).[43,44] They do not have a plasmon resonance in the visible region, as compared to other MXenes, which have characteristic plasmon resonances from the near-UV to mid-IR.[8] Their conductivity is not significantly affected by intercalants,

unlike all other MXenes.[45] Moreover, due to their atomically thicker nature, it is expected that their bending rigidity will allow them to keep a planar shape in suspended membranes, cantilevers, or polymer-matrix composites, exceeding all other 2D materials.[46,47] Mo_4VC_4 has recently found its first application as a nanotherapeutic agent against MRSA infection.[48] Following the synthesis of Mo_4VAlC_4 and Mo_4VC_4, it was demonstrated that $n = 4$ was possible; however, it was unknown whether more MAX-phases (and subsequent MXenes) could be synthesized.

The theoretical design of MAX-phases (and subsequent MXenes) is possible through Density Functional Theory (DFT) calculations. Stable MAX-phases can be predicted by modeling their enthalpy of formation and comparing that against competing MAX-phases. For instance, the experimental synthesis of Mo_2ScAlC_2 was achieved by theoretically modeling the successful phase, despite its single-M derivatives being unstable (Mo_3AlC_2 and Sc_3AlC_2).[31] The first i-MAX-phase $(Mo_{2/3}Sc_{1/3})_2AlC$ was used as a basis for the theoretical modeling and experimental verification of several novel i-MAX-phases including $(V_{2/3}Zr_{1/3})_2AlC$ and $(Mo_{2/3}Y_{1/3})_2AlC$.[49] Theoretical models such as this allow for accurate prediction of previously unattainable MAX-phase families and open the possibility for hundreds of theoretically possible MXenes.

Herein, we report two new phase-pure M_5AX_4 MAX-phases: $Ti_{2.5}Ta_{2.5}AlC_4$ and $Ti_{2.675}Nb_{2.325}AlC_4$. For clarity, the reported MXenes (and accompanying MAX-phases) will be referred to as $(M'M'')_5C_4$. The structural analysis found that $(TiTa)_5C_4$ shares the same herring-bone type structure as Mo_4VC_4, indicating this structure may be characteristic of the M_5X_4 family. Optical and thermal analyses show promising properties not found in other MXenes, and the use of DFT to successfully predict stable MAX-phases shows promise for expanding the M_5X_4 family.

RESULTS & DISCUSSION
Synthesis and Structural Characterization

To find new M_5AX_4 MAX-phases, metal powder precursors were mixed in M'_x:M''_{5-x} ratios where $x = 1, 2, 2.5, 3,$ or 4. Each chemistry was tested with 5 at% of one of the corresponding metallic oxides (see Supporting Information for a complete list of tested chemistries). Following ball-milling with zirconia balls, the powders were sintered at 1650 °C for 24 hours under Ar. The products were characterized via powder X-ray diffraction (XRD). It was determined that, of the chemistries tested, the following yielded two new phase-pure M_5AX_4 MAX phases: $Ti_{2.5}Ta_{2.5}AlC_4$ (using TiO_2; listed as $(TiTa)_5AlC_4$), $Ti_{2.675}Nb_{2.325}AlC_4$ (using Nb_2O_5; listed as $(TiNb)_5AlC_4$). It may be the case that the use of oxides in synthesis results in oxygen dissolution in the carbon sublattice, forming oxycarbides[50] and stabilizing the structure, however, this will not be investigated in depth in this article. After the discovery of $(TiTa)_5AlC_4$ and $(TiNb)_5AlC_4$, DFT calculations were employed to confirm the stability of $(TiTa)_5AlC_4$ and $(TiNb)_5AlC$ as well as to predict the stability of other M_5AX_4 MAX-phases. Details of DFT calculations are discussed later in this manuscript. We experimentally tested the compositions that were predicted stable using the same metal-oxide ratios, which did not yield another M_5AX_4 MAX-phase. However, we discovered a series of new solid-solution compositions, such as $(TiTa)_2AlC$ and $(TaV)_2AlC$[51], and alternate synthesis methods for preexisting MAX-phases such as $(TiNb)_4AlC_3$, $(VNb)_4AlC_3$, and $(TiV)_2AlC$ (Figures S1-17, Table S1). These MAX phases were not used for MXene synthesis in this work but represent a broad selection of novel solid-solution MAX phases and consequent MXenes for future study.

To synthesize multilayer MXene, HCl-washed MAX powders were etched with hydrofluoric acid (HF) to selectively etch out the A layer. The process of optimizing the synthesis can be found in Figure S18. It was found that the optimal etching time was nine days for $(TiTa)_5AlC_4$ and seven days for $(TiNb)_5AlC_4$; these gave the highest yield without over-etching.

3

For analysis, the multilayer sediment was collected via vacuum-assisted filtration and dried at 25 °C.
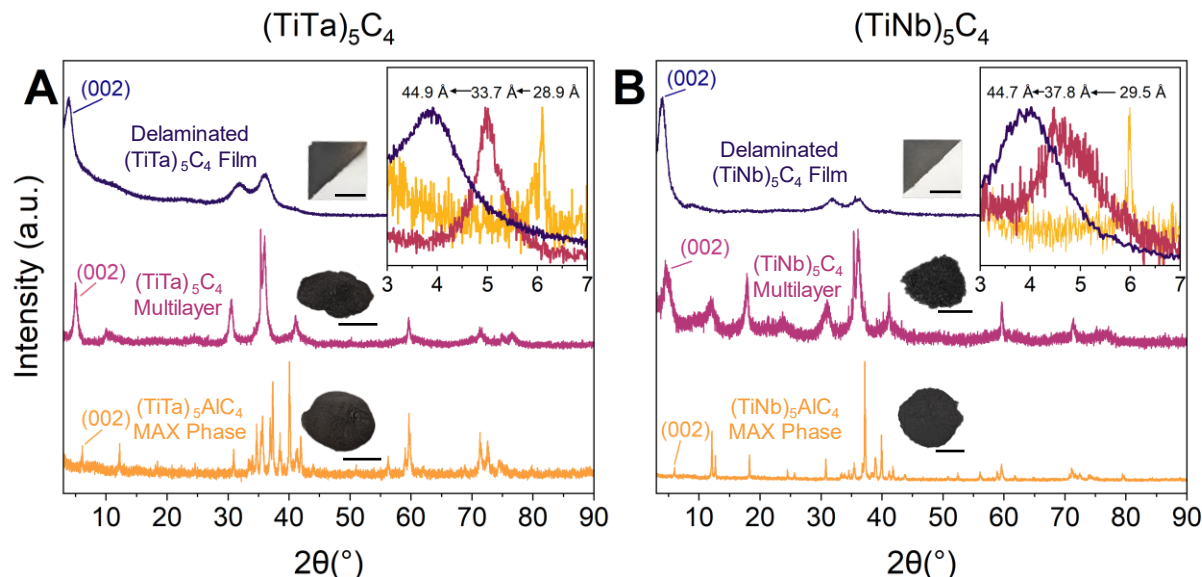

Figure 2. X-ray diffraction (XRD) patterns of (A) $(TiTa)_5C_4$ and (B) $(TiNb)_5C_4$ MAX, multilayer MXene, and delaminated MXene film with labeled (002) peaks. Insets show optical pictures of corresponding powders/spray-coated films. The scale bars on each image are 1 cm. Inset graphs show the (002) peak shift and the corresponding change in the c-lattice parameter.

Figure 2 shows an XRD analysis of the parent MAX phase, as well as the derived MXenes. For $(TiTa)_5AlC_4$, the (002) peak occurs at 6.10°, corresponding to a c-lattice parameter of 28.9 Å; for $(TiNb)_5AlC_4$, the (002) peak occurs at 5.98° (c-lattice parameter of 29.5 Å), which is the largest c-lattice parameter of any known MAX-phase.[36] Both are larger than the previously reported Mo_4VAlC_4 (28.22 Å) due to the larger ion size of both Ta and Nb in $(TiTa)_5AlC_4$ and $(TiNb)_5AlC_4$. The use of HF to selectively etch the A-layer resulted in the (002) peak shifting to lower 2θ for both, indicating the expansion along the c-lattice as a result of the A-layer removal.[44] Delamination of the multilayer MXenes was done by intercalating tetramethylammonium hydroxide (TMAOH) between the MXene sheets.[14] This was performed at both 25 °C and 35 °C; delaminated MXene from the 35 °C delamination was used for further analysis. For both MXenes, delamination only occurred when the dried multilayer powders were redispersed in the aqueous solution; delamination directly after etching and washing did not yield MXene but a light brown solution. For $(TiTa)_5C_4$, delamination occurred at both temperatures, with the average flake size increasing at higher temperatures (Figure S21); however $(TiNb)_5C_4$ did not yield MXene at room temperature, suggesting stronger interactions between the MXene sheets. The longer etching time of $(TiTa)_5C_4$ contributed to minor defects in the MXene sheets, likely resulting in weaker interactions between the flakes, which allowed for delamination at a lower temperature (Figure S23). As seen in Figure 2, the delamination of multilayer powder resulted in another shift of the (002) peaks towards lower 2θ values and a broadening of the peaks, resulting from the semi-random flakes alignment in the films.

Figure 3 shows the microscopic characterization of $(TiNb)_5AlC_4$ and $(TiNb)_5C_4$, where visual indication of etching can be observed (Figure S23 for corresponding $(TiTa)_5C_4$ data). The expansion of the layers between the SEM micrographs in Figure 3A and 3C is indicative of Al

4

removal from the MAX. This can be seen on the atomic level in the HR-TEM images (Figure 3B and 3D), where the brighter lines represent the Al layers. Their absence in the post-etching image is visual proof of the selective removal of the A-layer while the 5-layered repeating MXene structure remains. The herringbone-type structure seen in Mo_4VC_4 was also observed in $(TiTa)_5C_4$ (Figure S23).[36] As the second example of this structure, the atomic arrangement may be characteristic of the M_5X_4 family as a more stable configuration. The $(TiNb)_5C_4$ MXene flake seen in Figure 3E is large enough to fold over itself, where the seam can be seen on the right side of the flake and non-overlapping sections can be seen on the left.
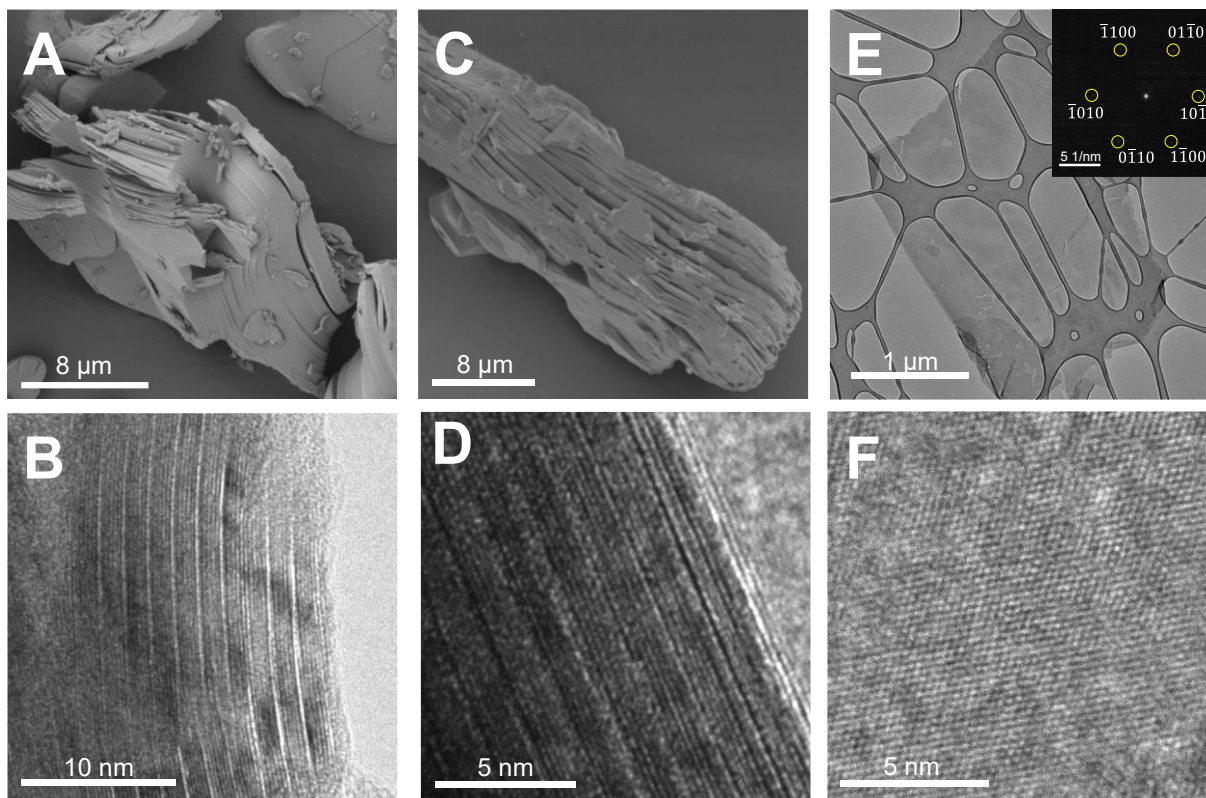
Figure 3. Microscopic analysis of $(TiNb)_5AlC_4$ and $(TiNb)_5C_4$. (A) scanning electron microscopy (SEM) micrograph of $(TiNb)_5AlC_4$ MAX phase particles. (B) Cross-sectional transmission electron microscopy (TEM) image showing the five-layered structure of $(TiNb)_5AlC_4$. The bright gray lines are the aluminum layers separating the five gray mixed-metal layers. (C) SEM micrograph of multilayer $(TiNb)_5C_4$ MXene showing increased gaps between layers indicating the selective etching and removal of the Al layer. (D) Cross-sectional TEM image showing a five-layered repeating structure of multilayer $(TiNb)_5C_4$ MXene. (E) In-plane TEM image of a large delaminated $(TiNb)_5C_4$ MXene flake folded in half on top of a lacey carbon grid with the hexagonal selected area electron diffraction (SAED) pattern of the [0001] zone axis in the inset. (F) HR-TEM image of the hexagonal atom arrangement in the basal plane of $(TiNb)_5C_4$ MXene.

Unfolded, the flake in Figure 3E would measure approximately 4.5 μm wide and 2 μm tall. This is larger than the average ~500 nm flake size recorded by DLS (Figure S21), showing that larger flake sizes are possible for $(TiNb)_5C_4$, indicating that increased stiffness relative to atomically thinner MXenes may lead to larger possible flake sizes.[52] On the other hand, $(TiTa)_5C_4$

showed flake sizes corresponding to the DLS flake measurements of ~300 nm (Figure S23). The SAED in Figure 3F corresponds to the hexagonal crystal structure as viewed from the [0001] zone axis, confirming that the carbide crystal structure was maintained during MXene synthesis. AFM (Figure S22) demonstrates an average flake thickness of 3.4 nm for $(TiNb)_5C_4$, apparently overestimating the thickness due to entrapped solvent molecules.[44]
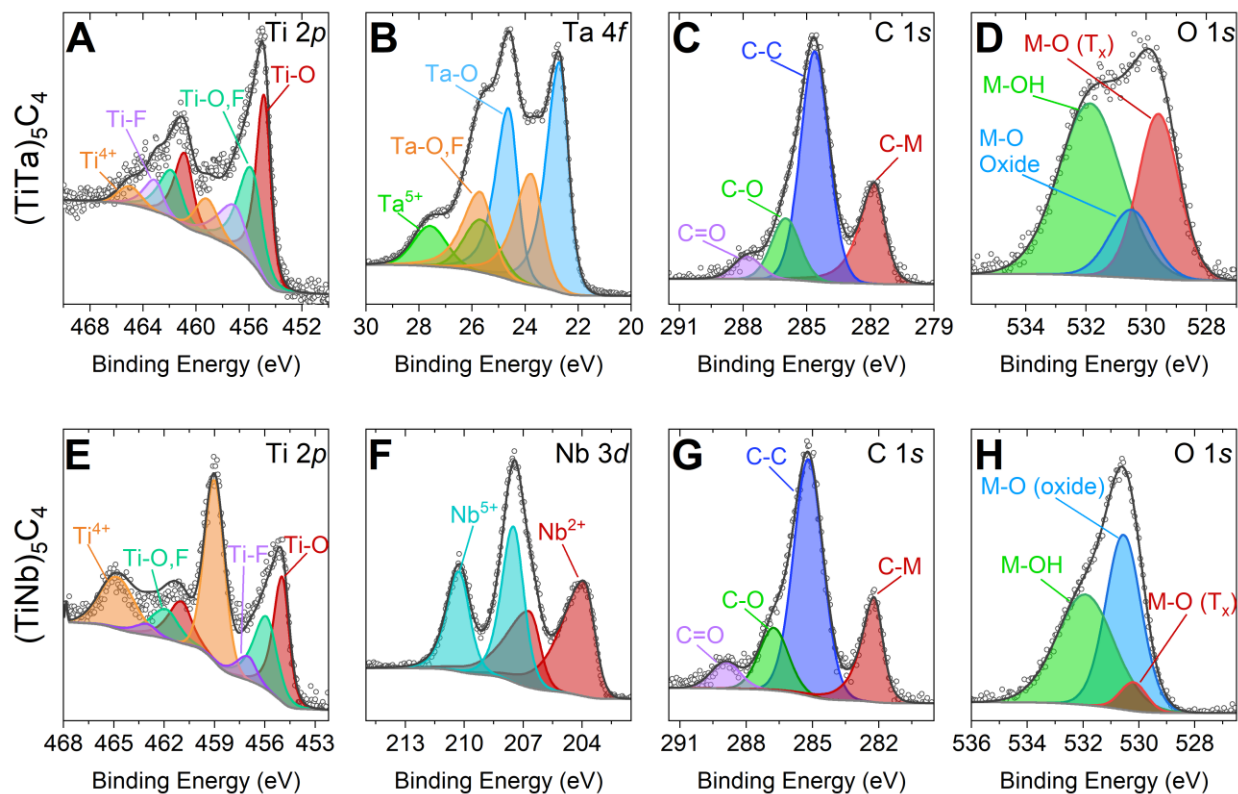
Compositional Characterization

Figure 4. High-resolution X-ray photoelectron spectroscopy (XPS) spectra of (top) $(TiTa)_5C_4$ and (bottom) $(TiNb)_5C_4$ free-standing films, showing (A, E) Ti 2p, (C, G) C 1s, (D, H) O 1s, (B) Ta 4f, and (F) Nb 3d core-level spectra.

Compositional characterization was carried out with both XPS (Figure 4) and EDS (Table S5). XPS indicated a slight titanium deficiency in both MXenes; however, EDS indicated that the ratio was approximately equivalent to initial stoichiometry amounts across all MAX and MXene stages. This may indicate a slight preferential ordering of titanium in the inner layers of the M_5X_4 unit cell, resulting in some of the titanium signal being blocked by the heavier metal in the outer layers. In $(TiTa)_5C_4$ this claim is further supported by the increased presence of oxygen over fluorine terminations, as tantalum preferentially bonds to oxygen. XPS shows the metal-carbon bond for both $(TiTa)_5C_4$ and $(TiNb)_5C_4$, confirming the MXene structure. The presence of the M-O peaks can indicate either sample oxidation or the presence of an oxycarbide. While unconfirmed, the requirement of oxide for successful M_5AX_4 MAX-phase synthesis may indicate that a small percentage of oxygen is needed to stabilize the lattice.
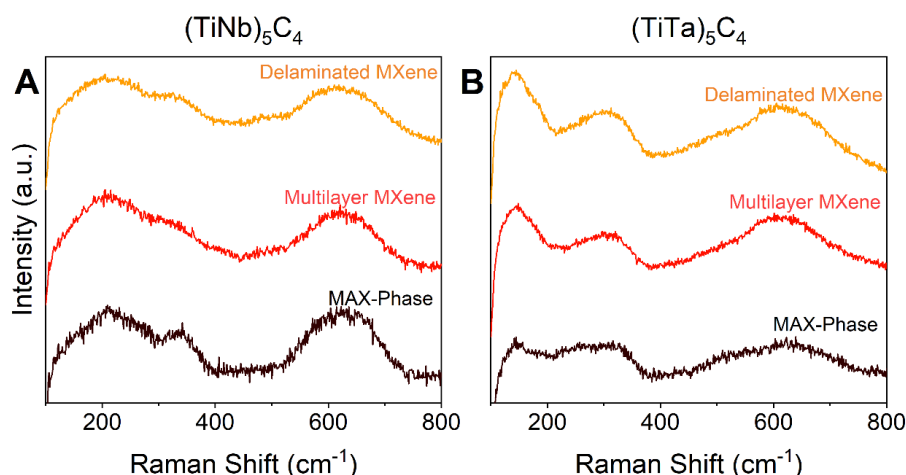
6

Figure 5. Raman spectra during each major synthesis step. (A) $(TiTa)_5C_4$ MAX and MXene spectra. (B) $(TiNb)_5C_4$ MAX and MXene spectra.

The Raman spectra of $(TiTa)_5AlC_4$ and $(TiNb)_5AlC_4$ MAX and $(TiTa)_5C_4$ and $(TiNb)_5C_4$ MXene in Figure 5 showed broad peaks below 1000 cm^{-1}, similar to the previously reported M_5X_4 MAX and MXene.[36] In the MAX spectra, the lack of signatures from Nb_2O_5 and TiO_2 precursors indicates complete reactions during the solid-state synthesis.[53,54] In both cases of $(TiTa)_5C_4$ and $(TiNb)_5C_4$ systems, the MAX and MXene have similar Raman spectra. The Raman peaks are broad compared to the single-transition-metal MAX phases and ordered MXenes, which are indicative of disorder due to the solid solution of transition metals.[55,56] Moreover, $(TiTa)_5C_4$ showed more broadening than $(TiNb)_5C_4$ due to the greater difference in atomic masses of the interchangeable elements. There are three peaks for each material, representing three groups of vibrations. The peak between 100 and 200 cm^{-1} represents the vibration of the transition metals, carbon, and surface groups. The peak in $(TiTa)_5C_4$ showed lower wavenumber than $(TiNb)_5C_4$, due to the heavier atoms. The following peaks in the 200 – 400 cm^{-1} region are typically assigned to the surface group vibrations, corresponding to the =O, –OH, and –F shown by XPS in Figure 4. The final peak is located in the 600 – 700 cm^{-1} region where both in and out-of-plane carbon vibrations are present. These peaks confirm the MXene structure and the absence of oxidation, as no signature of relevant oxides was found in the same region. The full spectrum (Figure S26) showed a broad peak between 1000 and 1500 cm^{-1} that belongs to amorphous carbon.[57] This typically arises from the degradation of PTFE stir bars due to extended stirring in hydrofluoric acid.

Optical Properties

The optical properties of both MXenes were measured by UV-vis-NIR spectrophotometry and Fourier transform infrared spectroscopy (FTIR). The UV-vis-NIR spectrophotometry was performed on a serially diluted MXene solution after delamination, which allowed for the calculation of the extinction coefficient from Beer's law (Table S8). Neither MXene showed distinct peaks in the UV or NIR ranges, indicating low optical activity in these ranges. Visually, the MXene solutions were both black (Figure S25). At 550 nm, the extinction coefficient (ε_{550}) was determined to be 18.7 L g^{-1} cm^{-1} for $(TiTa)_5C_4$ and 20.9 L $g^{-1}cm^{-1}$ for $(TiNb)_5C_4$, both lower

than the ε_{550} reported for Mo_4VC_4 of 34.4 L $g^{-1}cm^{-1}$, making these the lowest recorded extinction coefficient for any MXene.[8,36] To further explore the optical properties, FTIR measurements were performed on spray-coated films from the same single-flake solution (Figure 6; see Figure 2 for optical images of the spray-coated films). The MXene samples were then characterized using Bruker Invenio FTIR Spectrometer in total reflectance mode to investigate their emissivity, which is important for assessing IR shielding performance. The results reveal that the emissivity of both $(TiNb)_5C_4$ and $(TiTa)_5C_4$ MXenes is significantly higher than that of the reference Ti_3C_2 MXene sample (with reflectance being respectively significantly lower). $(TiNb)_5C_4$ showed slightly higher emissivity (and respectively lower in reflectivity) than $(TiTa)_5C_4$, indicating that the increase in atomic thickness as well as the addition of Nb and Ta in the MXene composition can lead to significant changes in their IR shielding properties. The unique IR shielding performance of M_5X_4 MXenes can be attributed to their electronic and structural properties. Further investigations are warranted to explore the full potential of M_5X_4 MXenes within IR shielding applications.
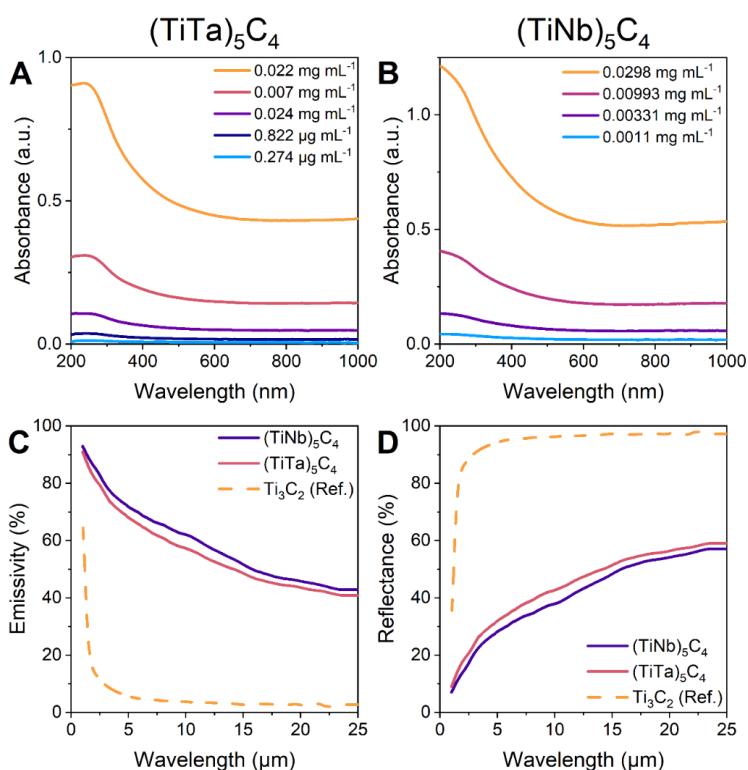

Figure 6. (A-B) UV-vis-NIR spectra of (A) $(TiTa)_5C_4$ and (B) $(TiNb)_5C_4$ MXene flakes in water, which were used to calculate the extinction coefficients. (C-D) FTIR spectra of spray-coated $(TiTa)_5C_4$ and $(TiNb)_5C_4$ films showing (C) emissivity and (D) reflectance compared to a Ti_3C_2 spray-coated reference film.

Thermal Stability

To investigate the thermal stability of both MAX-phase and multilayer MXene powders, thermogravimetric analysis (TGA) (Figure 7) coupled with residual gas analysis (RGA) was conducted (Figure S28). Both M_5AX_4 MAX phases show similar thermal stability to stoichiometric Ti_3AlC_2 MAX with the onset of oxidation under air at ~600 °C.[58] Further analysis of the weight gain, based on the large difference in molecular weight of Ti and Ta, also suggests

that $(TiTa)_5AlC_4$ MAX contains little oxygen substitution in the carbon lattice (discussed in the Supporting Information). We speculate that the presence of a small amount of oxide is necessary to nucleate the formation of the MAX phases, where the oxygen is present in the carbon lattice initially and helps stabilize the structure.

Thicker MXene sheets with more atomic layers are expected to be more thermally stable because their structures are closer to that of cubic carbides with a greater number of strong M-X bonds. However, compared to Ti_3C_2, both M_5X_4 MXenes do not show improved stability, and instead show decomposition starting at ~450 °C under both inert and oxidizing atmospheres. Under air, two processes occur simultaneously, weight gain from oxidation of the metal and weight loss from pyrolysis of the carbon (Figure S28). Thus, a greater total weight loss from $(TiNb)_5C_4$ indicates that this sample is likely more defective than $(TiTa)_5C_4$. TEM analysis indicates that both samples contain point defects resulting from over-etching due to the harsh etching conditions (long time, high temperature, and high HF concentration) (Figure S23F). XPS analysis indicates that the Ti in $(TiNb)_5C_4$ sample is more oxidized than the Ti in $(TiTa)_5C_4$, and there is a greater amount of adventitious carbon, which indicates the $(TiNb)_5C_4$ is more defective. Moreover, $(TiNb)_5C_4$ exhibits a higher weight loss from chemisorbed water (up to ~300 °C) with a first signature of CO_2 at a lower temperature (~225 °C) compared to $(TiTa)_5C_4$, which indicates a more defective MXene (Figures S29,30). Considering that the final transition under an inert atmosphere occurs at ~900 °C for both MXenes, the thermal stability of non-defective M_5X_4 MXenes may indeed be higher than atomically thinner MXene structures. However, further improvements in the synthesis process are necessary to confirm this.
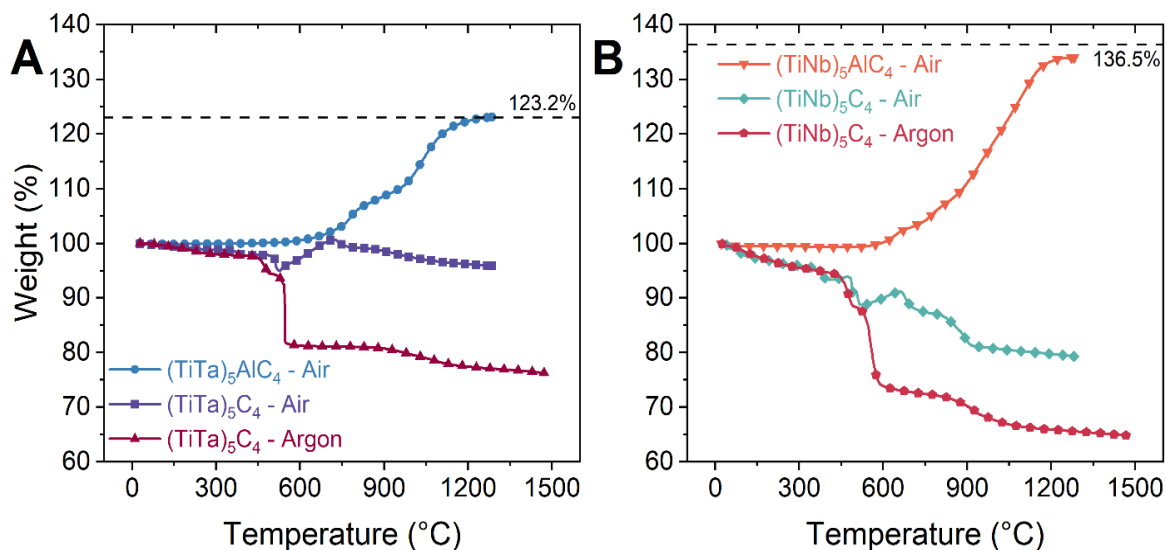

Figure 7. Thermogravimetric analysis of (A) $(TiTa)_5C_4$ and (B) $(TiNb)_5C_4$ MAX and MXenes under air and argon. The dashed line indicates the theoretical weight gain for the MAX under Air.

DFT Calculations

Following the discovery of $(TiTa)_5AlC_4$ and $(TiNb)_5AlC_4$, we used DFT to search for other stable M_5AX_4 MAX-phases. To predict the stability for $\left(M'_{1-y}M''_y\right)_5AlC_4$ systems, two different crystal structures were considered, (i) the traditional MAX phase structure (space group $P6_3/mmc$) and (ii) the recently reported twinned structure (space group $P\text{-}6m2$).[36] For each crystal structure,

we have considered M´ and M´´ in a random arrangement, to mimic solid solution disorder, and with out-of-plane chemical order. The ordered arrangements considered are illustrated in Figure 8. For each composition, we solve the linear optimization problem, identify the equilibrium simplex, and calculate the stability ΔG_{cp} (Eq. 1). Note that all phases which have been modeled with solid solution disorder, $\left(M'_{1-y}M''_{y}\right)_5 AlC_4$ as well as competing phases including $\left(M'_{1-y}M''_{y}\right)_{n+1}AlC_n$ with n = 1, 2, 3, have a contribution from configurational entropy to their Gibbs free energy (Eq.2 and 3).
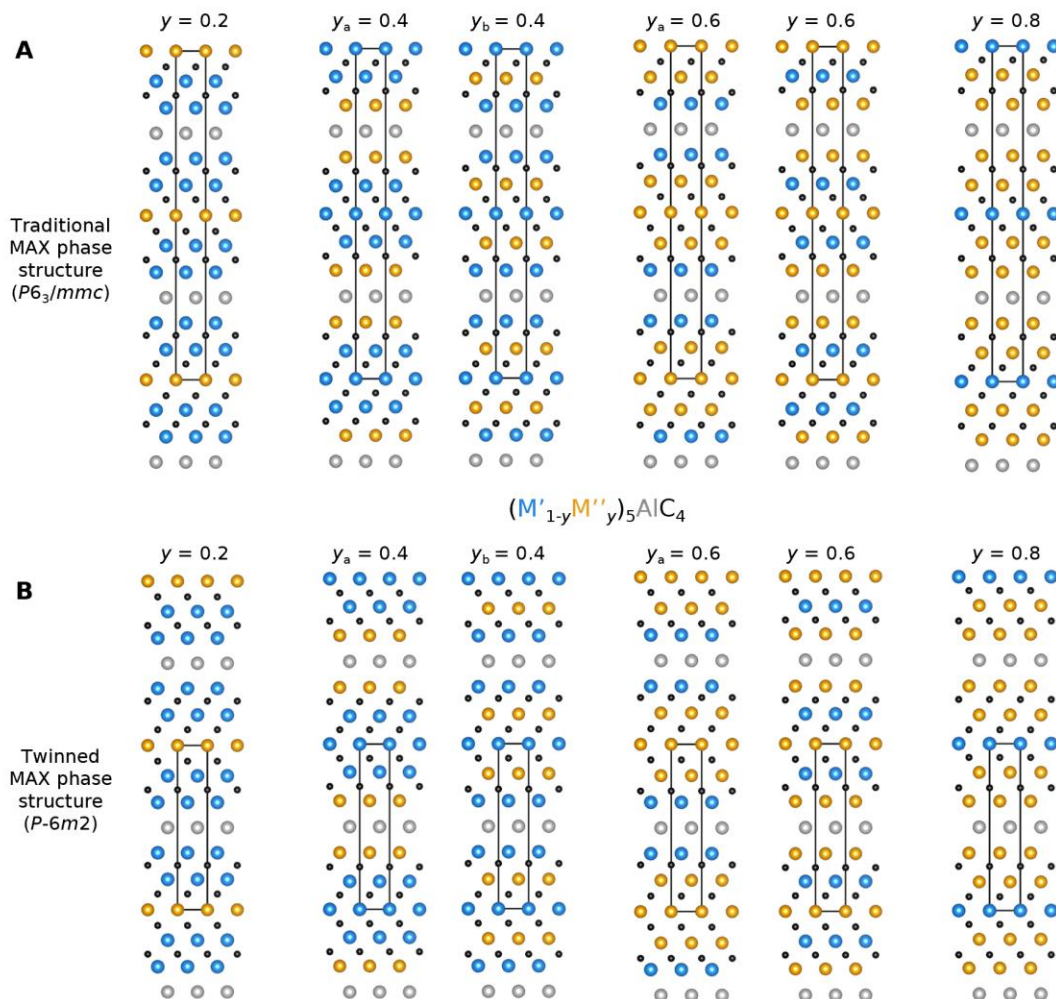

Figure 8. Schematic illustration of ordered arrangements considered for $\left(M'_{1-y}M''_{y}\right)_5 AlC_4$ systems using (a) the traditional MAX-phase structure with space group $P6_3/mmc$ and (b) a twinned structure with space group $P\text{-}6m2$. M´ atoms in blue, M´´ in orange, Al in grey, and C in black.

Figure 9 shows the calculated Gibbs free energy of formation (estimated at 2000 K) for 10 different $\left(M'_{1-y}M''_{y}\right)_5 AlC_4$ systems. Five of these systems (TiV, TiNb, TiTa, TaV, ScMo) have compositions predicted stable, with $\Delta G_{cp} < 0$, while the others are identified as close stable with $0 \leq \Delta G_{cp} \leq 50$. Solid solution disorder with the $P6_3/mmc$ structure is predicted stable for $(Ti_{0.4}V_{0.6})_5 AlC_4$ in Figure 9A, $(Ti_{1-y}Nb_y)_5 AlC_4$ in Figure 9B $(0.4 \leq y \leq 0.8)$, $(Ti_{1-y}Ta_y)_5 AlC_4$ in

10

Figure 9E ($0.2 \leq y \leq 0.8$), and $(Sc_{1-y}Mo_y)_5AlC_4$ in Figure 9J ($0.4 \leq y \leq 0.6$). In some of these systems, the twinned P-$6m2$ structure is also found to be stable but less so than the traditional MAX phase structure. Focusing on the solid solution disordered arrangements, the $P6_3/mmc$ structure is mostly lower in energy than P-$6m2$. However, the P-$6m2$ is found to be more favored in Mo-based systems as shown in Figure 9DGHI.

Solid solution disorder is typically lower in energy than herein considered ordered arrangements. However, in Mo-based systems, it is found that chemical order is favored, as seen in Figure 9DGHIJ. Out of these ordered structures, 3 are predicted stable. One in the $P6_3/mmc$ structure, $Mo_3Sc_2AlC_4$ ($y_b = 0.6$ in Figure 9J), and two in the twinned P-$6m2$ structure, $Mo_3Ti_2AlC_4$ and $Mo_3Sc_2AlC_4$ ($y_b = 0.6$ in Figure 9H,J). Other ordered Mo-based structures are found close to stable, i.e. with $0 \leq \Delta G_{cp} \leq 50$. It should be noted that all three stable phases have an ordered arrangement where Mo is located both in the middle layer and next to the Al layer. This arrangement is marked as $y_b = 0.6$ in Figure 9. Furthermore, we have considered ideal structures with M-, A-, and X-sites being fully occupied, i.e., no vacancies have been considered. The impact of defects, such as vacancies, may stabilize these phases further. Any deviation in the theoretical stability predictions and the experimentally derived MAX-phases may be due to the addition of oxides during synthesis.
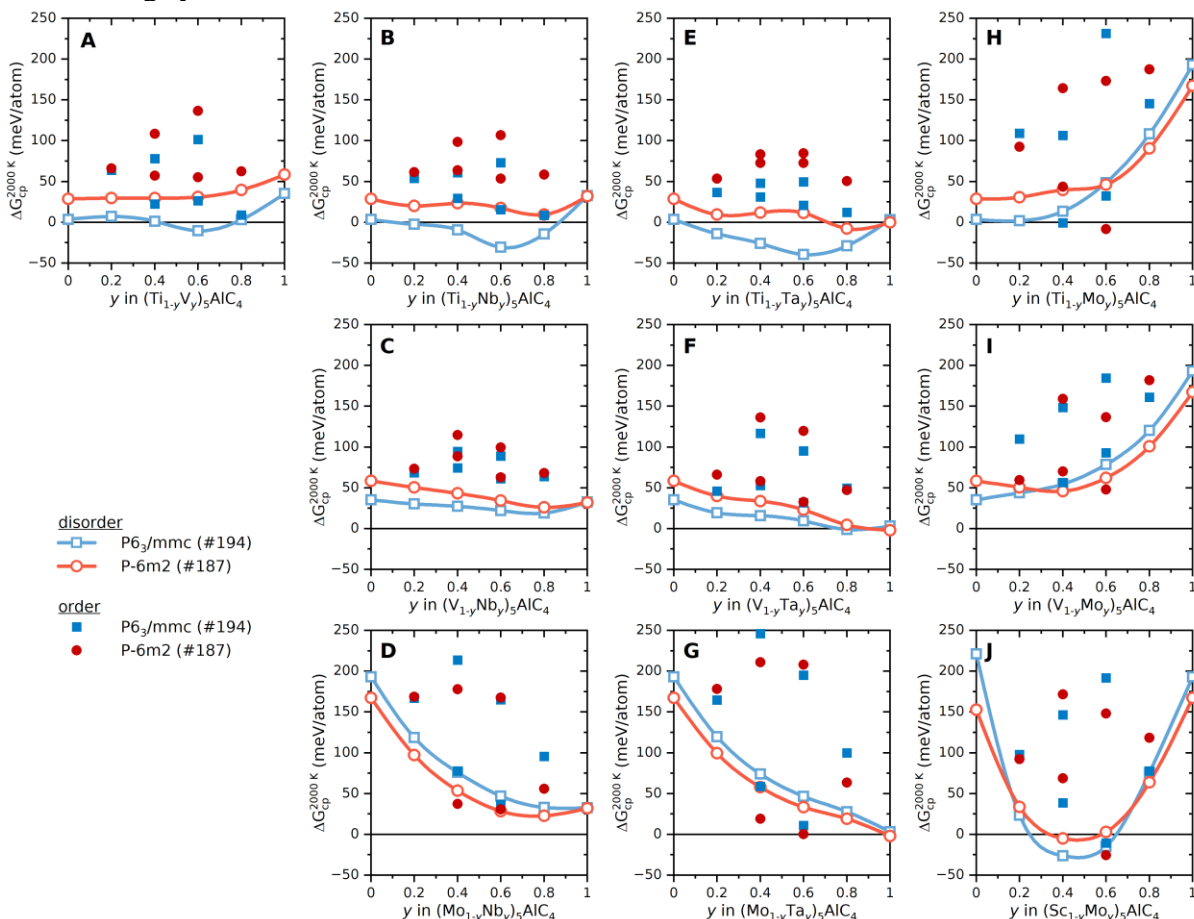

Figure 9. Calculated stability at 2000 K, $\Delta G_{cp}^{2000\,K}$, for different quaternary $(M'_{1-y}M''_y)_5AlC_4$ as a function of x assuming the traditional MAX-phase structure with space group $P6_3/mmc$ (blue squares) or a twinned structure with space group P-$6m2$ (red circles). The distribution of M' and

11

M´´ on the M-sites have been considered with a random arrangement to mimic solid solution disorder (filled symbols) and as out-of-plane order (open symbols).

CONCLUSION

The successful synthesis of $(TiTa)_5C_4$ and $(TiNb)_5C_4$ establishes the M_5X_4 family beyond Mo_4VC_4. $(TiTa)_5C_4$ and $(TiNb)_5C_4$ were both confirmed to be disordered solid solutions on the M-site and $(TiTa)_5C_4$ was confirmed to exhibit the same twinned structure found in Mo_4VC_4, indicating this structure may be a hallmark of the M_5X_4 family. The studied MXenes demonstrate exciting thermal and optical properties not found in other MXenes, making them a promising candidate for optoelectronics, electrochemical, and high-temperature applications. The successful use of DFT predictions to isolate stable MAX-phases has the possibility to map other favorable M_5AX_4 MAX-phases to further expand the MXene family. These reported MAX-phases and MXenes comprise an established M_5X_4 family that can be successfully synthesized and isolated to be phase-pure.

EXPERIMENTAL

Synthesis of $Ti_{2.5}Ta_{2.5}AlC_4$ and $Ti_{2.675}Nb_{2.325}C_4$ MAX Phases

Titanium (IV) (~325 mesh, 99.5% metals basis), titanium (IV) oxide, niobium (~325 mesh, 99.8% metals basis), niobium (V) oxide (99.5% metals basis), tantalum (~325 mesh, 99.9% metals basis, 99.6%), tantalum (V) oxide (99% metals basis), molybdenum (~250 mesh, 99.9% metals basis), molybdenum (VI) oxide (99.5%), vanadium (~325 mesh, 99.5%), vanadium (V) oxide (99.2%), aluminum (~325 mesh, 99.5% (metals basis)), and graphite (~325 mesh, 99%) powders were combined in varying atomic ratios (see Supporting Information) and ball-milled for 12 hours at a ratio of 1:2 = powder: yttria-stabilized zirconia (YSZ) balls by weight. The mixtures were then heated in alumina crucibles at 3 °C min^{-1} to 1650 °C under 350 cm^3 min^{-1} flowing argon in a tube furnace (Carbolite Gero) and held for 24 hours before cooling to room temperature, also at 3 °C min^{-1}. The sintered materials were then ground to powder using a mortar and pestle. The resulting MAX-phases were stirred in 9M Hydrochloric Acid for 12 hours to dissolve metallic impurities, then washed to neutral pH by vacuum filtration with water. The powders were collected and dried overnight at room temperature under vacuum. The powders were then sieved using stainless-steel meshes to obtain a particle size of <75 μm.

Synthesis of $Ti_{2.5}Ta_{2.5}C_4$ and $Ti_{2.675}Nb_{2.325}C_4$ MXenes

To synthesize multilayer MXenes, 6 grams of MAX powders were slowly added to 60 mL of HF (48-51% Arcos Organics) while being stirred with a polytetrafluoroethylene (PTFE)-coated stir bar at 400 rpm. For the synthesis of $(TiTa)_5C_4$, the reaction was carried out for 9 days, while for the synthesis of $(TiNb)_5C_4$, the reaction was carried out for 7 days. Both reactions were held at 50 °C in a mineral oil bath. After completion, the samples were washed via a series of cycles involving centrifugation at 3,500 rpm (2,550 rcf) for 10 minutes, decanting the acidic supernatant, and redispersion of the sediment using deionized (DI) water until the supernatant reached a neutral pH. The multilayer MXene powder was then collected by vacuum-assisted filtration through a porous membrane (MF-Millipore 0.45 μm Mixed Cellulose Ester).

To produce delaminated MXene flakes, 1 g of multilayer $(TiTa)_5C_4$ or $(TiNb)_5C_4$ MXene powders were dispersed in 20 mL of 10 wt % tetramethylammonium hydroxide (TMAOH, 25 wt % - diluted to 10 wt %, Sigma Aldrich), and stirred at 400 rpm for 24 h at 35°C. TMAOH was then washed out through a series of cycles involving centrifugation at 10,000 rpm (12,850 rcf) for

12

10 min, discarding the supernatant, and redispersing the sediment with DI water. A paint shaker was used to redisperse the sediment because it adhered strongly to the walls of the centrifuge tube. This process was repeated until the supernatant had a pH < 8. From here, the sediment was redispersed in DI water, shaken for 30 minutes, then centrifuged at 3,500 rpm (2,550 rcf) for 30 minutes. The resulting black supernatant was carefully decanted to collect the delaminated MXene. This process was repeated twice to collect approximately 300 mL of MXene. The concentration of the single-flake solution was determined by drop-casting 100 μL of the solution onto oven-dried silicon wafers, drying, and measuring the weight change.

Film Preparation

To obtain free-standing films, the delaminated MXene flake colloid was filtered via vacuum-assisted filtration through a porous membrane (Celgard 3501, 64 nm pore size, polypropylene). The resulting films were separated from the Celgard and stored in a vacuum desiccator at room temperature.

Structural Characterization

The crystal structures of all powders were characterized by XRD. Rigaku SmartLab (40 kV/30 mA) and MiniFlex (40 kV/15 mA) X-ray diffractometers were used with Ni-filtered Cu K_α radiation. The step size of the scan was 0.01° with a step duration of 4 s for MAX-phase powders and 2 s for the multilayer MXene powders and films.

The flake size and zeta potential were determined with a Malvern Zetasizer NanoZS Dynamic Light Scattering (DLS) instrument using a disposable capillary cell. Three measurements were taken per sample and averaged for the final flake size.

Microscopy

SEM micrographs were obtained with a Zeiss Supra 50VP scanning electron microscope. Transmission electron microscopy (TEM), scanning transmission electron microscopy (STEM), selected area electron diffraction (SAED), and Energy Dispersive Spectroscopy (EDS) were performed on a JEOL 2100F FEG microscope operating at 200 kV. Samples were prepared from colloids containing the MAX-phase powders and MXene powders/flakes were drop-cast onto lacy carbon copper grids. AFM was performed on drop-cast MXene flakes on silicon wafers with a dioxide layer using Bruker Multimode 8 with a Si tip (Budget Sensors Tap300Al-G; $f_0 = 300$ kHz, $k = 40$ N m^{-1}) in tapping mode in air.

Chemical Composition

X-ray photoelectron spectra were collected using a spectrometer (Versa Probe 5000, Physical Electronics) equipped with a monochromatic Al K_α X-ray source with a 200 μm spot size. Charge neutralization was performed using a dual-beam setup supplying low-energy electrons and Ar$^+$ ions. High-resolution spectra were collected at a pass energy of 23.5 eV with a step size of 0.05 eV, whereas the survey spectra were collected at a pass energy of 117 eV with a step size of 0.5 eV. The quantification and curve fitting of the core-level spectra were performed using Casa XPS software package with Shirley-type backgrounds. The carbon-metal component at 282.0 eV in the C 1*s* spectra was used for binding energy scale correction.

Raman spectra were obtained using an inverted reflection mode spectrometer (Renishaw inVia) with a 63× (NA = 0.7) objective, diffraction-based room-temperature detector, and 633 nm laser with an 1800 line/mm grating. The laser power was in the ~0.5−1 mW range.

Optical Properties

UV-vis-NIR spectra were collected using a Thermo Scientific Evolution 201 spectrometer in transmission mode from 200 to 1000 nm. Samples were prepared by serial dilution of delaminated MXene solutions with DI water and measured in quartz cuvettes (1 cm path length and water for blank measurement). The extinction was normalized to path length and plotted against concentration to find the extinction coefficient according to the Beer-Lambert equation ($A = \varepsilon b C$). FTIR spectra were obtained using spray-coated MXene films on glass substrates. Surface roughness of MXene films was obtained using an optical profiler (Keyence VK-X1050 with a 785 nm laser).

The FTIR measurements were performed using the Bruker Invenio Spectrometer in Total Reflectance mode. The resolution was set to 4 cm^{-1} with 14 scans total, and the Opus software was used to apply smoothing with 5 points average. Measurements were taken at room temperature and average humidity. Gold-coated mirror was used as a reference background, and the background was respectively subtracted for each sample at 1 to 25 µm range.

Thermal Analysis

The high-temperature behavior of MAX-phase and multilayer MXene powders was studied using thermogravimetric analysis (SDT 650, TA Instruments) coupled with evolved gas analysis (Discovery mass spectrometer, TA Instruments). Powders with masses around 15 mg were packed in a 90 µL alumina pan and heated to 1300 °C (under 100 mL min^{-1} dry airflow) or 1500 °C (under 300 mL min^{-1} Ar flow) at 20 °C min^{-1}.

DFT Calculations

All first-principles calculations were performed by means of density functional theory (DFT) and the projector augmented wave method,[59,60] as implemented within the Vienna ab-initio simulation package (VASP) version 5.4.1.[61–63] We used the non-spin polarized generalized gradient approximation (GGA) as parameterized by Perdew–Burke–Ernzerhof (PBE) for treating the electron exchange and correlation effects.[64]

To model chemical disorder of M′ and M′′ on the *M* sublattice for $\left(\mathrm{M'}_{1-y}\mathrm{M''}_y\right)_{n+1}\mathrm{AlC}_n$ with $n = 1$ to 4, we used the special quasi-random structure (SQS) method[65] to generate supercells composed of 72 to 256 atoms. Convergency tests in previous works show that the supercells used give a qualitatively accurate representation and a quantitative convergence in terms of calculated formation enthalpies and lattice parameters.[66,67]

The thermodynamic stability of quaternary MAX phases was investigated at 2000 K with respect to decomposition into any combination of competing phases. The set of most competing phases, denoted equilibrium simplex, is identified using a linear optimization procedure [68,69] which has been proven successful in confirming already experimentally known MAX phases as well as predicting the existence of new ones.[19,49,66,67,69–73] The stability of the quaternary MAX phase is quantified in terms of the formation Gibbs free energy ΔG_{cp} by comparing its energy to the energy of the equilibrium simplex using

$$\Delta G_{\mathrm{cp}} = G\left(\left(\mathrm{M'}_{1-y}\mathrm{M''}_y\right)_5\mathrm{AlC}_4\right) - G(\text{equilibrium simplex}). \qquad (1)$$

A phase is concluded stable when $\Delta G_{\mathrm{cp}} < 0$ or at best metastable for $\Delta G_{\mathrm{cp}} > 0$. Note that since we evaluate the stability at 2000 K, configurational entropy will decrease the Gibbs free energy if the phase is considered with a solid solution disorder. This is the case both for

14

$(M'_{1-y}M''_y)_5AlC_4$ as well as for competing phases like lower-order MAX phases $(M'_{1-y}M''_y)_2AlC$, $(M'_{1-y}M''_y)_3AlC_2$, and $(M'_{1-y}M''_y)_4AlC_3$. The contribution from configurational entropy due to the disorder of M´ and M´´ on the M sublattices will decrease the Gibbs free energy G^{disorder} as approximated by

$$G^{\text{disorder}}[T] = H^{\text{disorder}} - T\Delta S, \qquad (2)$$

where the entropic contribution ΔS, assuming an ideal solution of M´ and M´´ on the M-sites, is given by

$$\Delta S = -\text{k}_B[y\ln(y) + (1-y)\ln(1-y)], \qquad (3)$$

where k_B is the Boltzmann constant, and x is the concentration of M´ on the M-sublattice.

Acknowledgments

References

(1) Naguib, M.; Kurtoglu, M.; Presser, V.; Lu, J.; Niu, J.; Heon, M.; Hultman, L.; Gogotsi, Y.; Barsoum, M. W. Two-Dimensional Nanocrystals Produced by Exfoliation of Ti_3AlC_2. *Adv. Mater.* **2011**, *23* (37), 4248–4253. https://doi.org/10.1002/adma.201102306.

(2) Anasori, B.; Naguib, M.; Guest Editors. Two-Dimensional MXenes. *MRS Bull.* **2023**, *48* (3), 238–244. https://doi.org/10.1557/s43577-023-00500-z.

(3) Kamysbayev, V.; Filatov, A. S.; Hu, H.; Rui, X.; Lagunas, F.; Wang, D.; Klie, R. F.; Talapin, D. V. Covalent Surface Modifications and Superconductivity of Two-Dimensional Metal Carbide MXenes. *Science* **2020**, *369* (6506), 979–983. https://doi.org/10.1126/science.aba8311.

(4) Zhang, C. (John); Anasori, B.; Seral-Ascaso, A.; Park, S.-H.; McEvoy, N.; Shmeliov, A.; Duesberg, G. S.; Coleman, J. N.; Gogotsi, Y.; Nicolosi, V. Transparent, Flexible, and Conductive 2D Titanium Carbide (MXene) Films with High Volumetric Capacitance. *Adv. Mater.* **2017**, *29* (36), 1702678. https://doi.org/10.1002/adma.201702678.

(5) Han, M.; Maleski, K.; Shuck, C. E.; Yang, Y.; Glazar, J. T.; Foucher, A. C.; Hantanasirisakul, K.; Sarycheva, A.; Frey, N. C.; May, S. J.; Shenoy, V. B.; Stach, E. A.; Gogotsi, Y. Tailoring Electronic and Optical Properties of MXenes through Forming Solid Solutions. *J. Am. Chem. Soc.* **2020**, *142* (45), 19110–19118. https://doi.org/10.1021/jacs.0c07395.

(6) Jastrzębska, A. M.; Szuplewska, A.; Wojciechowski, T.; Chudy, M.; Ziemkowska, W.; Chlubny, L.; Rozmysłowska, A.; Olszyna, A. In Vitro Studies on Cytotoxicity of

Delaminated Ti$_3$C$_2$ MXene. *J. Hazard. Mater.* **2017**, *339*, 1–8.
https://doi.org/10.1016/j.jhazmat.2017.06.004.

(7) Hantanasirisakul, K.; Zhao, M.-Q.; Urbankowski, P.; Halim, J.; Anasori, B.; Kota, S.; Ren, C. E.; Barsoum, M. W.; Gogotsi, Y. Fabrication of Ti$_3$C$_2$T$_x$ MXene Transparent Thin Films with Tunable Optoelectronic Properties. *Adv. Electron. Mater.* **2016**, *2* (6), 1600050. https://doi.org/10.1002/aelm.201600050.

(8) Maleski, K.; Shuck, C. E.; Fafarman, A. T.; Gogotsi, Y. The Broad Chromatic Range of Two-Dimensional Transition Metal Carbides. *Adv. Opt. Mater.* **2021**, *9* (4), 2001563. https://doi.org/10.1002/adom.202001563.

(9) Li, X.; Huang, Z.; Shuck, C. E.; Liang, G.; Gogotsi, Y.; Zhi, C. MXene Chemistry, Electrochemistry and Energy Storage Applications. *Nat. Rev. Chem.* **2022**, *6* (6), 389–404. https://doi.org/10.1038/s41570-022-00384-8.

(10) Li, H.; Fan, R.; Zou, B.; Yan, J.; Shi, Q.; Guo, G. Roles of MXenes in Biomedical Applications: Recent Developments and Prospects. *J. Nanobiotechnology* **2023**, *21* (1), 73. https://doi.org/10.1186/s12951-023-01809-2.

(11) Zhang, D.; Shah, D.; Boltasseva, A.; Gogotsi, Y. MXenes for Photonics. *ACS Photonics* **2022**, *9* (4), 1108–1116. https://doi.org/10.1021/acsphotonics.2c00040.

(12) Iqbal, A.; Sambyal, P.; Koo, C. M. 2D MXenes for Electromagnetic Shielding: A Review. *Adv. Funct. Mater.* **2020**, *30* (47). https://doi.org/10.1002/adfm.202000883.

(13) VahidMohammadi, A.; Rosen, J.; Gogotsi, Y. The World of Two-Dimensional Carbides and Nitrides (MXenes). *Science* **2021**, *372* (6547), eabf1581. https://doi.org/10.1126/science.abf1581.

(14) Lim, K. R. G.; Shekhirev, M.; Wyatt, B. C.; Anasori, B.; Gogotsi, Y.; Seh, Z. W. Fundamentals of MXene Synthesis. *Nat. Synth.* **2022**, *1* (8), 601–614. https://doi.org/10.1038/s44160-022-00104-6.

(15) Mashtalir, O.; Naguib, M.; Mochalin, V. N.; Dall'Agnese, Y.; Heon, M.; Barsoum, M. W.; Gogotsi, Y. Intercalation and Delamination of Layered Carbides and Carbonitrides. *Nat. Commun.* **2013**, *4* (1), 1716. https://doi.org/10.1038/ncomms2664.

(16) Naguib, M.; Unocic, R. R.; Armstrong, B. L.; Nanda, J. Large-Scale Delamination of Multi-Layers Transition Metal Carbides and Carbonitrides "MXenes." *Dalton Trans.* **2015**, *44* (20), 9353–9358. https://doi.org/10.1039/C5DT01247C.

(17) Wang, D.; Zhou, C.; Filatov, A. S.; Cho, W.; Lagunas, F.; Wang, M.; Vaikuntanathan, S.; Liu, C.; Klie, R. F.; Talapin, D. V. Direct Synthesis and Chemical Vapor Deposition of 2D Carbide and Nitride MXenes. *Science* **2023**, *379* (6638), 1242–1247. https://doi.org/10.1126/science.add9204.

(18) Naguib, M.; Halim, J.; Lu, J.; Cook, K. M.; Hultman, L.; Gogotsi, Y.; Barsoum, M. W. New Two-Dimensional Niobium and Vanadium Carbides as Promising Materials for Li-Ion Batteries. *J. Am. Chem. Soc.* **2013**, *135* (43), 15966–15969. https://doi.org/10.1021/ja405735d.

(19) Tao, Q.; Dahlqvist, M.; Lu, J.; Kota, S.; Meshkian, R.; Halim, J.; Palisaitis, J.; Hultman, L.; Barsoum, M. W.; Persson, P. O. Å.; Rosen, J. Two-Dimensional Mo$_{1.33}$C MXene with Divacancy Ordering Prepared from Parent 3D Laminate with in-Plane Chemical Ordering. *Nat. Commun.* **2017**, *8* (1), 14949. https://doi.org/10.1038/ncomms14949.

(20) Soundiraraju, B.; George, B. K. Two-Dimensional Titanium Nitride (Ti$_2$N) MXene: Synthesis, Characterization, and Potential Application as Surface-Enhanced Raman

Scattering Substrate. *ACS Nano* **2017**, *11* (9), 8892–8900.
https://doi.org/10.1021/acsnano.7b03129.

(21) Urbankowski, P.; Anasori, B.; Hantanasirisakul, K.; Yang, L.; Zhang, L.; Haines, B.; May, S. J.; Billinge, S. J. L.; Gogotsi, Y. 2D Molybdenum and Vanadium Nitrides Synthesized by Ammoniation of 2D Transition Metal Carbides (MXenes). *Nanoscale* **2017**, *9* (45), 17722–17730. https://doi.org/10.1039/C7NR06721F.

(22) Meshkian, R.; Näslund, L.-Å.; Halim, J.; Lu, J.; Barsoum, M. W.; Rosen, J. Synthesis of Two-Dimensional Molybdenum Carbide, Mo_2C, from the Gallium Based Atomic Laminate Mo 2 Ga 2 C. *Scr. Mater.* **2015**, *108*, 147–150.
https://doi.org/10.1016/j.scriptamat.2015.07.003.

(23) Meshkian, R.; Dahlqvist, M.; Lu, J.; Wickman, B.; Halim, J.; Thörnberg, J.; Tao, Q.; Li, S.; Intikhab, S.; Snyder, J.; Barsoum, M. W.; Yildizhan, M.; Palisaitis, J.; Hultman, L.; Persson, P. O. Å.; Rosen, J. W-Based Atomic Laminates and Their 2D Derivative $W_{1.33}C$ MXene with Vacancy Ordering. *Adv. Mater.* **2018**, *30* (21), 1706409.
https://doi.org/10.1002/adma.201706409.

(24) Persson, I.; el Ghazaly, A.; Tao, Q.; Halim, J.; Kota, S.; Darakchieva, V.; Palisaitis, J.; Barsoum, M. W.; Rosen, J.; Persson, P. O. Å. Tailoring Structure, Composition, and Energy Storage Properties of MXenes from Selective Etching of In-Plane, Chemically Ordered MAX Phases. *Small* **2018**, *14* (17), 1703676. https://doi.org/10.1002/smll.201703676.

(25) Halim, J.; Palisaitis, J.; Lu, J.; Thörnberg, J.; Moon, E. J.; Precner, M.; Eklund, P.; Persson, P. O. Å.; Barsoum, M. W.; Rosen, J. Synthesis of Two-Dimensional $Nb_{1.33}C$ (MXene) with Randomly Distributed Vacancies by Etching of the Quaternary Solid Solution $(Nb_{2/3}Sc_{1/3})_2AlC$ MAX Phase. *ACS Appl. Nano Mater.* **2018**, *1* (6), 2455–2460.
https://doi.org/10.1021/acsanm.8b00332.

(26) Anasori, B.; Gogotsi, Y. MXenes: Trends, Growth, and Future Directions. *Graphene 2D Mater.* **2022**, *7* (3), 75–79. https://doi.org/10.1007/s41127-022-00053-z.

(27) Naguib, M.; Mashtalir, O.; Carle, J.; Presser, V.; Lu, J.; Hultman, L.; Gogotsi, Y.; Barsoum, M. W. Two-Dimensional Transition Metal Carbides. *ACS Nano* **2012**, *6* (2), 1322–1331.
https://doi.org/10.1021/nn204153h.

(28) Zhou, J.; Zha, X.; Zhou, X.; Chen, F.; Gao, G.; Wang, S.; Shen, C.; Chen, T.; Zhi, C.; Eklund, P.; Du, S.; Xue, J.; Shi, W.; Chai, Z.; Huang, Q. Synthesis and Electrochemical Properties of Two-Dimensional Hafnium Carbide. *ACS Nano* **2017**, *11* (4), 3841–3850.
https://doi.org/10.1021/acsnano.7b00030.

(29) Zhou, J.; Zha, X.; Chen, F. Y.; Ye, Q.; Eklund, P.; Du, S.; Huang, Q. A Two-Dimensional Zirconium Carbide by Selective Etching of Al3C3 from Nanolaminated $Zr_3Al_3C_5$. *Angew. Chem. Int. Ed.* **2016**, *55* (16), 5008–5013. https://doi.org/10.1002/anie.201510432.

(30) Anasori, B.; Xie, Y.; Beidaghi, M.; Lu, J.; Hosler, B. C.; Hultman, L.; Kent, P. R. C.; Gogotsi, Y.; Barsoum, M. W. Two-Dimensional, Ordered, Double Transition Metals Carbides (MXenes). *ACS Nano* **2015**, *9* (10), 9507–9516.
https://doi.org/10.1021/acsnano.5b03591.

(31) Meshkian, R.; Tao, Q.; Dahlqvist, M.; Lu, J.; Hultman, L.; Rosen, J. Theoretical Stability and Materials Synthesis of a Chemically Ordered MAX Phase, Mo_2ScAlC_2, and Its Two-Dimensional Derivate Mo_2ScC_2 MXene. *Acta Mater.* **2017**, *125*, 476–480.
https://doi.org/10.1016/j.actamat.2016.12.008.

(32) Yang, J.; Naguib, M.; Ghidiu, M.; Pan, L.-M.; Gu, J.; Nanda, J.; Halim, J.; Gogotsi, Y.; Barsoum, M. W. Two-Dimensional Nb-Based M_4C_3 Solid Solutions (MXenes). *J. Am. Ceram. Soc.* **2016**, *99* (2), 660–666. https://doi.org/10.1111/jace.13922.

(33) Urbankowski, P.; Anasori, B.; Makaryan, T.; Er, D.; Kota, S.; Walsh, P. L.; Zhao, M.; Shenoy, V. B.; Barsoum, M. W.; Gogotsi, Y. Synthesis of Two-Dimensional Titanium Nitride Ti_4N_3 (MXene). *Nanoscale* **2016**, *8* (22), 11385–11391. https://doi.org/10.1039/C6NR02253G.

(34) Tran, M. H.; Schäfer, T.; Shahraei, A.; Dürrschnabel, M.; Molina-Luna, L.; Kramm, U. I.; Birkel, C. S. Adding a New Member to the MXene Family: Synthesis, Structure, and Electrocatalytic Activity for the Hydrogen Evolution Reaction of $V_4C_3T_x$. *ACS Appl. Energy Mater.* **2018**, *1* (8), 3908–3914. https://doi.org/10.1021/acsaem.8b00652.

(35) Ghidiu, M.; Naguib, M.; Shi, C.; Mashtalir, O.; Pan, L. M.; Zhang, B.; Yang, J.; Gogotsi, Y.; Billinge, S. J. L.; Barsoum, M. W. Synthesis and Characterization of Two-Dimensional Nb_4C_3 (MXene). *Chem Commun* **2014**, *50* (67), 9517–9520. https://doi.org/10.1039/C4CC03366C.

(36) Deysher, G.; Shuck, C. E.; Hantanasirisakul, K.; Frey, N. C.; Foucher, A. C.; Maleski, K.; Sarycheva, A.; Shenoy, V. B.; Stach, E. A.; Anasori, B.; Gogotsi, Y. Synthesis of Mo_4VAlC_4 MAX Phase and Two-Dimensional Mo_4VC_4 MXene with Five Atomic Layers of Transition Metals. *ACS Nano* **2020**, *14* (1), 204–217. https://doi.org/10.1021/acsnano.9b07708.

(37) Kurtoglu, M.; Naguib, M.; Gogotsi, Y.; Barsoum, M. W. First Principles Study of Two-Dimensional Early Transition Metal Carbides. *MRS Commun.* **2012**, *2* (4), 133–137. https://doi.org/10.1557/mrc.2012.25.

(38) Tan, T. L.; Jin, H. M.; Sullivan, M. B.; Anasori, B.; Gogotsi, Y. High-Throughput Survey of Ordering Configurations in MXene Alloys Across Compositions and Temperatures. *ACS Nano* **2017**, *11* (5), 4407–4418. https://doi.org/10.1021/acsnano.6b08227.

(39) Ahmed, B.; Ghazaly, A. E.; Rosen, J. I-MXenes for Energy Storage and Catalysis. *Adv. Funct. Mater.* **2020**, *30* (47), 2000894. https://doi.org/10.1002/adfm.202000894.

(40) Hong, W.; Wyatt, B. C.; Nemani, S. K.; Anasori, B. Double Transition-Metal MXenes: Atomistic Design of Two-Dimensional Carbides and Nitrides. *MRS Bull.* **2020**, *45* (10), 850–861. https://doi.org/10.1557/mrs.2020.251.

(41) Sun, W.; Wang, H.-W.; Vlcek, L.; Peng, J.; Brady, A. B.; Osti, N. C.; Mamontov, E.; Tyagi, M.; Nanda, J.; Greenbaum, S. G.; Kent, P. R. C.; Naguib, M. Multiscale and Multimodal Characterization of 2D Titanium Carbonitride MXene. *Adv. Mater. Interfaces* **2020**, *7* (11), 1902207. https://doi.org/10.1002/admi.201902207.

(42) Pinto, D.; Anasori, B.; Avireddy, H.; Shuck, C. E.; Hantanasirisakul, K.; Deysher, G.; Morante, J. R.; Porzio, W.; Alshareef, H. N.; Gogotsi, Y. Synthesis and Electrochemical Properties of 2D Molybdenum Vanadium Carbides – Solid Solution MXenes. *J. Mater. Chem. A* **2020**, *8* (18), 8957–8968. https://doi.org/10.1039/D0TA01798A.

(43) Seredych, M.; Shuck, C. E.; Pinto, D.; Alhabeb, M.; Precetti, E.; Deysher, G.; Anasori, B.; Kurra, N.; Gogotsi, Y. High-Temperature Behavior and Surface Chemistry of Carbide MXenes Studied by Thermal Analysis. *Chem. Mater.* **2019**, *31* (9), 3324–3332. https://doi.org/10.1021/acs.chemmater.9b00397.

(44) Shekhirev, M.; Shuck, C. E.; Sarycheva, A.; Gogotsi, Y. Characterization of MXenes at Every Step, from Their Precursors to Single Flakes and Assembled Films. *Prog. Mater. Sci.* **2021**, *120*, 100757. https://doi.org/10.1016/j.pmatsci.2020.100757.

(45) Hart, J. L.; Hantanasirisakul, K.; Lang, A. C.; Anasori, B.; Pinto, D.; Pivak, Y.; van Omme, J. T.; May, S. J.; Gogotsi, Y.; Taheri, M. L. Control of MXenes' Electronic Properties through Termination and Intercalation. *Nat. Commun.* **2019**, *10* (1), 522. https://doi.org/10.1038/s41467-018-08169-8.

(46) Lipatov, A.; Lu, H.; Alhabeb, M.; Anasori, B.; Gruverman, A.; Gogotsi, Y.; Sinitskii, A. Elastic Properties of 2D $Ti_3C_2T_x$ MXene Monolayers and Bilayers. *Sci. Adv.* **2018**, *4* (6), eaat0491. https://doi.org/10.1126/sciadv.aat0491.

(47) Lipatov, A.; Alhabeb, M.; Lu, H.; Zhao, S.; Loes, M. J.; Vorobeva, N. S.; Dall'Agnese, Y.; Gao, Y.; Gruverman, A.; Gogotsi, Y.; Sinitskii, A. Electrical and Elastic Properties of Individual Single-Layer $Nb_4C_3T_x$ MXene Flakes. *Adv. Electron. Mater.* **2020**, *6* (4), 1901382. https://doi.org/10.1002/aelm.201901382.

(48) Liu, Y.; He, X.; Feng, J.; Wang, D.; Obeng, E.; Yu, C.; Song, Y.; Shen, J.; Li, Z. Engineering A New Member of MXenes M_5C_4 Phases Nanoplatforms as Synergistically Photothermal and Chemodynamic Therapeutics for Methicillin-Resistant Staphylococcus Aureus. *Chem. Eng. J.* **2023**, 143004. https://doi.org/10.1016/j.cej.2023.143004.

(49) Dahlqvist, M.; Lu, J.; Meshkian, R.; Tao, Q.; Hultman, L.; Rosen, J. Prediction and Synthesis of a Family of Atomic Laminate Phases with Kagomé-like and in-Plane Chemical Ordering. *Sci. Adv.* **2017**, *3* (7), e1700642. https://doi.org/10.1126/sciadv.1700642.

(50) Michałowski, P. P.; Anayee, M.; Mathis, T. S.; Kozdra, S.; Wójcik, A.; Hantanasirisakul, K.; Jóźwik, I.; Piątkowska, A.; Możdżonek, M.; Malinowska, A.; Diduszko, R.; Wierzbicka, E.; Gogotsi, Y. Oxycarbide MXenes and MAX Phases Identification Using Monoatomic Layer-by-Layer Analysis with Ultralow-Energy Secondary-Ion Mass Spectrometry. *Nat. Nanotechnol.* **2022**, *17* (11), 1192–1197. https://doi.org/10.1038/s41565-022-01214-0.

(51) Nowotny, H.; Rogl, P.; Schuster, J. C. Structural Chemistry of Complex Carbides and Related Compounds. *J. Solid State Chem.* **1982**, *44* (1), 126–133. https://doi.org/10.1016/0022-4596(82)90409-1.

(52) Shekhirev, M.; Busa, J.; Shuck, C. E.; Torres, A.; Bagheri, S.; Sinitskii, A.; Gogotsi, Y. Ultralarge Flakes of $Ti_3C_2T_x$ MXene via Soft Delamination. *ACS Nano* **2022**, *16* (9), 13695–13703. https://doi.org/10.1021/acsnano.2c04506.

(53) Raba, A. M.; Bautista-Ruíz, J.; Joya, M. R. Synthesis and Structural Properties of Niobium Pentoxide Powders: A Comparative Study of the Growth Process. *Mater. Res.* **2016**, *19*, 1381–1387. https://doi.org/10.1590/1980-5373-MR-2015-0733.

(54) Mazza, T.; Barborini, E.; Piseri, P.; Milani, P.; Cattaneo, D.; Li Bassi, A.; Bottani, C. E.; Ducati, C. Raman Spectroscopy Characterization of TiO_2 Rutile Nanocrystals. *Phys. Rev. B* **2007**, *75* (4), 045416. https://doi.org/10.1103/PhysRevB.75.045416.

(55) Gouadec, G.; Colomban, P. Raman Spectroscopy of Nanomaterials: How Spectra Relate to Disorder, Particle Size and Mechanical Properties. *Prog. Cryst. Growth Charact. Mater.* **2007**, *53* (1), 1–56. https://doi.org/10.1016/j.pcrysgrow.2007.01.001.

(56) Presser, V.; Naguib, M.; Chaput, L.; Togo, A.; Hug, G.; Barsoum, M. W. First-Order Raman Scattering of the MAX Phases: Ti_2AlN, $Ti_2AlC_{0.5}N_{0.5}$, Ti_2AlC, $(Ti_{0.5}V_{0.5})_2AlC$, V_2AlC, Ti_3AlC_2, and Ti_3GeC_2. *J. Raman Spectrosc.* **2012**, *43* (1), 168–172. https://doi.org/10.1002/jrs.3036.

(57) Pelletier, M. J. *Analytical Applications of Raman Spectroscopy*; Blackwell science Oxford, 1999; Vol. 427.

(58) Mathis, T. S.; Maleski, K.; Goad, A.; Sarycheva, A.; Anayee, M.; Foucher, A. C.; Hantanasirisakul, K.; Shuck, C. E.; Stach, E. A.; Gogotsi, Y. Modified MAX Phase Synthesis for Environmentally Stable and Highly Conductive Ti_3C_2 MXene. *ACS Nano* **2021**, *15* (4), 6420–6429. https://doi.org/10.1021/acsnano.0c08357.

(59) Blöchl, P. E. Projector Augmented-Wave Method. *Phys. Rev. B* **1994**, *50* (24), 17953–17979. https://doi.org/10.1103/PhysRevB.50.17953.

(60) Kresse, G.; Joubert, D. From Ultrasoft Pseudopotentials to the Projector Augmented-Wave Method. *Phys. Rev. B* **1999**, *59* (3), 1758–1775. https://doi.org/10.1103/PhysRevB.59.1758.

(61) Kresse, G.; Hafner, J. Ab Initio Molecular Dynamics for Liquid Metals. *Phys. Rev. B* **1993**, *47* (1), 558–561. https://doi.org/10.1103/PhysRevB.47.558.

(62) Kresse, G.; Furthmüller, J. Efficiency of Ab-Initio Total Energy Calculations for Metals and Semiconductors Using a Plane-Wave Basis Set. *Comput. Mater. Sci.* **1996**, *6* (1), 15–50. https://doi.org/10.1016/0927-0256(96)00008-0.

(63) Kresse, G.; Furthmüller, J. Efficient Iterative Schemes for Ab Initio Total-Energy Calculations Using a Plane-Wave Basis Set. *Phys. Rev. B* **1996**, *54* (16), 11169–11186. https://doi.org/10.1103/PhysRevB.54.11169.

(64) Perdew, J. P.; Burke, K.; Ernzerhof, M. Generalized Gradient Approximation Made Simple. *Phys. Rev. Lett.* **1996**, *77* (18), 3865–3868. https://doi.org/10.1103/PhysRevLett.77.3865.

(65) Zunger, A.; Wei, S.-H.; Ferreira, L. G.; Bernard, J. E. Special Quasirandom Structures. *Phys. Rev. Lett.* **1990**, *65* (3), 353–356. https://doi.org/10.1103/PhysRevLett.65.353.

(66) Dahlqvist, M.; Rosen, J. Predictive Theoretical Screening of Phase Stability for Chemical Order and Disorder in Quaternary 312 and 413 MAX Phases. *Nanoscale* **2020**, *12* (2), 785–794. https://doi.org/10.1039/C9NR08675G.

(67) Dahlqvist, M.; Rosen, J. The Rise of MAX Phase Alloys – Large-Scale Theoretical Screening for the Prediction of Chemical Order and Disorder. *Nanoscale* **2022**, *14* (30), 10958–10971. https://doi.org/10.1039/D2NR02414D.

(68) Dahlqvist, M.; Alling, B.; Abrikosov, I. A.; Rosén, J. Phase Stability of Ti_2C upon Oxygen Incorporation: A First-Principles Investigation. *Phys. Rev. B* **2010**, *81* (2), 024111. https://doi.org/10.1103/PhysRevB.81.024111.

(69) Dahlqvist, M.; Alling, B.; Rosén, J. Stability Trends of MAX Phases from First Principles. *Phys. Rev. B* **2010**, *81* (22), 220102. https://doi.org/10.1103/PhysRevB.81.220102.

(70) Dai, Y.; Gao, J.; Huang, L.; Ding, R.; Wang, P.; Yang, F. First-Principles Study of Resistive Random Access Memory Based on Single-Layer Black Phosphorous Resistive Layer. *J. Appl. Phys.* **2020**, *128* (21), 215702. https://doi.org/10.1063/5.0024513.

(71) Thore, A.; Dahlqvist, M.; Alling, B.; Rosén, J. First-Principles Calculations of the Electronic, Vibrational, and Elastic Properties of the Magnetic Laminate Mn_2GaC. *J. Appl. Phys.* **2014**, *116* (10), 103511. https://doi.org/10.1063/1.4894411.

(72) Ingason, A. S.; Petruhins, A.; Dahlqvist, M.; Magnus, F.; Mockute, A.; Alling, B.; Hultman, L.; Abrikosov, I. A.; Persson, P. O. Å.; Rosen, J. A Nanolaminated Magnetic Phase: Mn_2GaC. *Mater. Res. Lett.* **2014**, *2* (2), 89–93. https://doi.org/10.1080/21663831.2013.865105.

(73) Dahlqvist, M.; Rosen, J. Order and Disorder in Quaternary Atomic Laminates from First-Principles Calculations. *Phys. Chem. Chem. Phys.* **2015**, *17* (47), 31810–31821. https://doi.org/10.1039/C5CP06021D.